Contents lists available at ScienceDirect

Palaeogeography, Palaeoclimatology, Palaeoecology

The evolution history of Asian monsoon and westerly winds over the past 14,000 years: Evidences from grain size of ash in the Hongyuan peat on the eastern Qinghai-Tibetan Plateau

Yongyong Bai [a], Mengxiu Zeng [a,*], Fengquan Li [a,*], Yougui Song [b], Yongqiu Wu [a], Jianghong Wu [a], Cheng Zhu [c], Haijun Peng [d], Hongjiao Wang [a], Zhigang Wang [a], Zhangrong Wu [a]

[a] College of Geography and Environmental Sciences, Zhejiang Normal University, Jinhua 321004, China
[b] State Key Laboratory of Loess and Quaternary Geology, Institute of Earth Environment, Chinese Academy of Sciences, Xi'an 710061, China
[c] School of Geographic and Oceanographic Sciences, Nanjing University, Nanjing 210023, China
[d] State Key Laboratory of Environmental Geochemistry, Institute of Geochemistry, Chinese Academy of Sciences, Guiyang 550081, China

ARTICLE INFO

ABSTRACT

The relationship between the Asian monsoon and westerly winds (WWs) on various temporal scales remains a topic of debate. The Zoige wetland, situated to the east of the Qinghai-Tibetan Plateau, is the largest highland wetland in China and highly sensitive to environmental changes. While several paleoenvironmental reconstructions have been conducted in this region, comprehensive investigations into grain size are still limited. In this study, we conducted a systematic investigation of grain size in ash from the sediments of the Hongyuan peat HY2014 profile in this area. The ash composition in this profile was primarily clay and silt particles, with a very low sand content. The grain size frequency curves generally exhibited a bimodal modality, except for the sediments in the bottom layers which displayed a single-peak pattern. By employing the end-member (EM) model and considering previous research findings, we reconstructed the atmospheric circulation since the last deglaciation. Three distinct EMs were identified. EM1 indicated long-distance suspended materials primarily transported by WWs. EM2 was associated with low-altitude circulation and linked to a decrease in the Asian summer monsoon (ASM). EM3 represented materials transported into the wetland via the Asian winter monsoon (AWM). Our results suggested that during the late deglacial period, characterized by strong AWM intensity, the Zoige wetland experienced cold and arid conditions. Moreover, the WWs and ASM exerted dominant influences, while the AWM gradually weakened during the Holocene, with variations in their intensities across different time intervals. The results also revealed a positive correlation between WWs and ASM, as well as a negative correlation between WWs and AWM.

1. Introduction

Atmospheric dust plays a pivotal role in shaping the intricate global climate system. It alters the radiation budget by absorbing and scattering solar radiation and outgoing terrestrial radiation, thereby influencing physical and biogeochemical interactions between the atmosphere, land surface, and ocean (Harrison et al., 2001). Furthermore, alterations in climatic conditions (such as precipitation, wind strength, and regional moisture balance) affect the emission, transport, and deposition of atmospheric dust (Harrison et al., 2001; Martini et al., 2006). Consequently, atmospheric dust acts as both an active instigator

and a passive chronicler of historical climate fluctuations. Peatlands serve as valuable archives that document atmospheric environmental changes and offer comprehensive reconstructions of palaeoclimate and paleoenvironmental variations. Within these peatland ecosystems, vegetation such as mosses can adeptly capture atmospheric dust, enabling peat archives to be extensively utilized in reconstructing the evolution history of atmospheric dust (Peng et al., 2021).

Mid-latitude westerly winds (WWs) and the Asian monsoon are two major atmospheric circulation patterns that exert a profound influence on climatic dynamics in the Northern Hemisphere. Nonetheless, the intricacies of their interrelationship in Asia and their respective

---

variabilities remain poorly understood. For example, Li et al. (2021) demonstrated a coherent paleo-precipitation pattern between the Asian summer monsoon (ASM) and WWs in the northeastern Qinghai Tibet Plateau (QTP) over millennium timescales. In contrast, Jia et al. (2018) suggested an out-of-phase association between WWs and the ASM during the Holocene in Central Asia. Previous reconstructions of the ASM and WWs based on the terrestrial archives such as stalagmites (Yang et al., 2019), lacustrine sediments (An et al., 2012; Bird et al., 2017), and loess-paleosol sequences (Jia et al., 2018; Jia et al., 2021, 2022) have unveiled some insights. However, there have been limited studies investigating their relationship using peat deposits, which serve as ideal archives for studying climate change, including the mechanisms and variability of Asian monsoon intensity (Ferrat et al., 2012; Zeng et al., 2022a). This gap in research exists due to constraints related to the distribution of peatlands and other considerations.

The eastern QTP is influenced by three climatic subsystems: the Asian winter monsoon (AWM), ASM, and WWs (An et al., 2018; An et al., 2012; Yu et al., 2011). Consequently, this region is an ideal area for studying the interactions among these climatic systems. The Hongyuan peat from the Zoige wetland in the eastern QTP can be dated to its early stage during the Holocene (Sun et al., 2017; Zhao et al., 2014), which allows for the reconstruction of Holocene climate change. Due to its proximity to prominent dust sources like the Taklimakan Desert, Loess Plateau, and QTP (Ferrat et al., 2012), the Zoige wetland can receive transported dust particles through the complex circulations of the Asian monsoon and WWs. The increased influence of non-local dust may indicate the strengthening of WWs and/or an increase in the strength or frequency of northerly cold fronts (Ferrat et al., 2012). Previous researches have established variations in precipitation and temperature within the Hongyuan peatland through the analysis of grayscale, humification (Wang et al., 2010), pollen (Yan et al., 2021; Zhou et al., 2010), and geochemical elements (Ferrat et al., 2012; Yu et al., 2011).
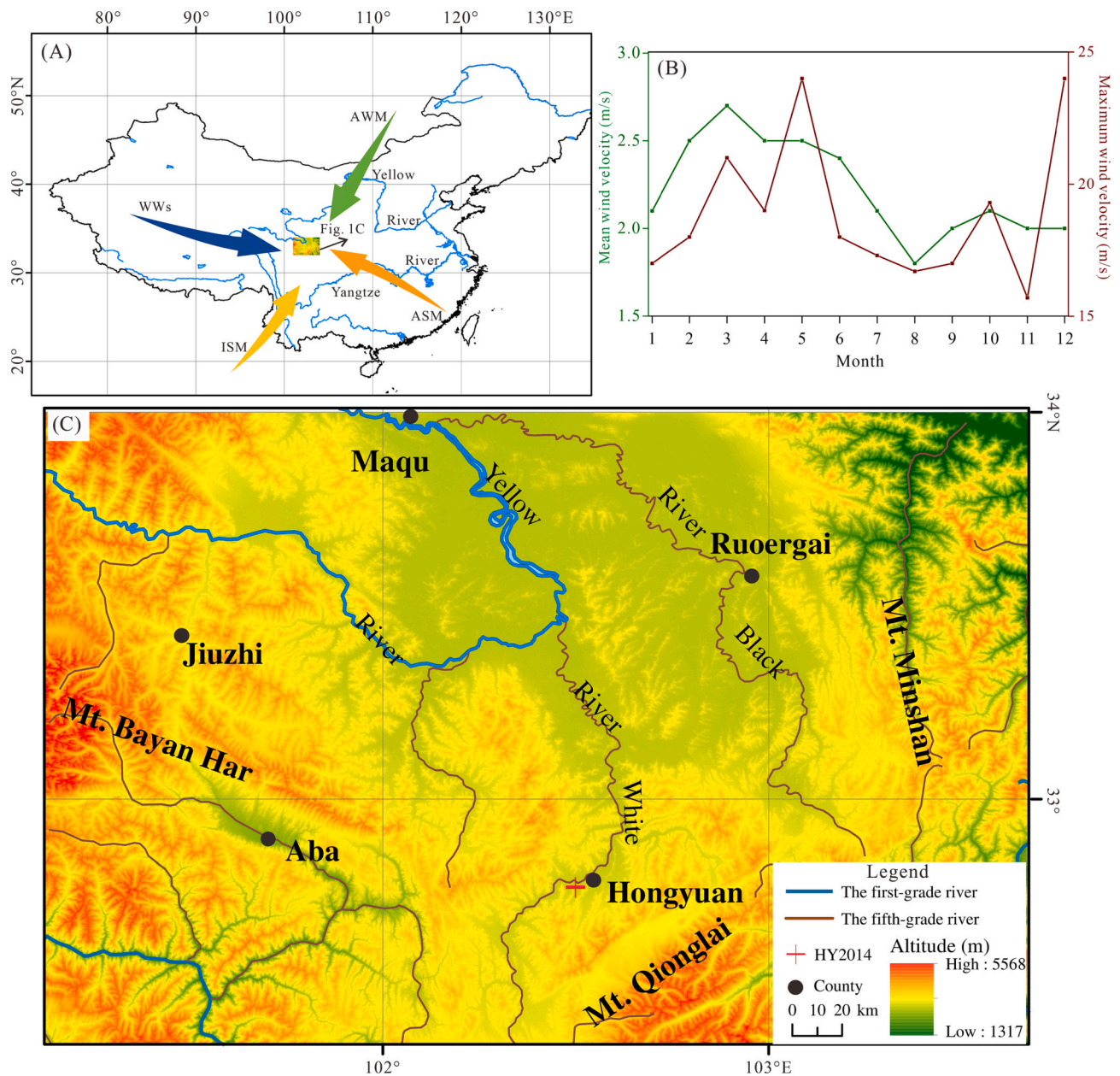
Fig. 1. Location and environmental context of the study region. (A) Location of the study region and the dominant circulation systems of the westerlies and Asian monsoons. (B) Monthly mean and maximum values of wind speed in Hongyuan County during the period of 1971 to 2000 CE. (C) The physical environment of the Zoige wetland and the specific location of the HY2014 profile.

However, previous research has given less attention to the dust records from the aspect of temporal evolution, and the contribution rates of each atmospheric circulation system, particularly the WWs to the Hongyuan area during the Holocene are still unknown.

To effectively reconstruct the historical atmospheric dust deposition in the Zoige wetland, understand the relationships among the AWM, the ASM, and WWs in the eastern QTP during the Holocene, and determine their respective contributions to atmospheric dust in each period, it becomes imperative to investigate indicators directly derived from atmospheric dust deposition. Here, we measured the grain size distribution in ash from the Hongyuan peat named the HY2014 profile in the Zoige wetland. This investigation was complemented by the utilization of particle grade-standard deviation, end-member (EM) model, and wavelet analysis to reconstruct the evolutionary history of atmospheric circulations since the last deglaciation, along with comprehending its underlying mechanisms. Our objectives were i) to interpret the environmental significance of each EM component of ash in the HY2014 profile based on the EM model, other mathematical analysis methods, and previous studies; ii) to reconstruct the climate and environmental evolution history of the study area; iii) to reveal the process of changes in atmospheric circulation and the underlying mechanism obtained from the unique study area since the last deglaciation.

2. Study area

The Hongyuan peatland (32°46′N, 102°30′E) located in the eastern part of the QTP, has developed a huge amount of ombrotrophic peat and is an important component of the largest wetland in China of the Zoige wetland (32°10′–34°10′N,101°45′–103°25′E, and ~3500 m asl) (Zeng et al., 2017) (Fig. 1A). The Zoige wetlands are strongly influenced by the Asian monsoon (Zeng et al., 2022b). During the summer season, this region is affected by the ASM and Indian summer monsoons (ISM), while the winter months are characterized by the influence of the WWs and AWM (Yu et al., 2011) (Fig. 1A). The QTP experiences strong winds that primarily from November to April of the following year, due to the impact of WWs, with monthly average wind speeds ranging from 1.8 m/ s to 2.7 m/s (Fig. 1B). The high altitude of the region results in an average annual temperature ranging from −1.7 °C to 3.3 °C. The mean annual precipitation varies from 650 mm to 750 mm, with approximately 80% of the rainfall occurring between May and September (Fig. S1).

In the high-altitude region with cold conditions, characterized by the development of meadows, the two predominant plant species that contribute to peat formation and cover the majority of Hongyuan County are *Carex muliensis* and *Kobresia humilis*. The frost period extends from October to the following April, resulting in a very short growing season for local vegetation, predominantly consisting of Cyperaceae. Towards the end of this brief growing period, Cyperaceae plants quickly die, and their slow decomposition in cold and dry environments contributes to the accumulation of peat material (Wang et al., 2010). The study region exhibits a unique location and topography, with mountains above 3800 m asl covered with alpine shrub meadow, whereas those between 3800 and 3000 m asl are characterized by alpine coniferous woods (Zhou et al., 2010). The Hongyuan peatland, which originated at least 10,300 yr BP, flourished during the early to mid-Holocene period (Sun et al., 2017; Zhao et al., 2014).

3. Materials and methods

3.1. Sampling and profile characteristics

A 450-cm-long peat profile HY2014 was obtained from a lowland piedmont ombrotrophic wetland (32°46′49.850″ N, 102°30′57. 047″E), located 2 km southwest of Hongyuan County in the southern Zoige wetland (Fig. 1C). The profile was quickly transported to the laboratory and stored refrigerated at 4 °C. The HY2014 profile can be divided into

seven stratigraphic layers according to peat colour and sedimentary characteristics (Zeng et al., 2017). Peat constituted the primary material, with two layers of pewter mud and silty clay at the bottom (Table S1). Plant material extracted from a total of 13 samples at various depths was measured by AMS^{14}C dating at the Xi'an Accelerator Mass Spectrometry Center, Institute of Earth Environment, Chinese Academy of Sciences. The ages were calibrated using the Calib 7.0.4 procedure with the Intcal13 calibration dataset (Reimer et al., 2013). Based on the Bacon method (Blaauw and Christen, 2011), a high-resolution geochronological framework was established, starting from 14,057 yr BP (Zeng et al., 2017). Details information about the samples and dating results are provided in Table S2. There was no age inversion or sedimentary discontinuity in this profile, making it an ideal carrier for the analysis of past atmospheric circulation.

3.2. Ash content and grain size measurement

A total of 226 samples were selected at a 2-cm interval for the HY2014 profile to conduct ash content and grain size analyses. To determine the ash content, the samples were dried at 105 °C for 12 h and subsequently ashed at 450 °C for another 12 h. The ash content was estimated as a percentage of the dry weight, and the mass fraction was calculated as the residual mass after burning. For grain size analysis, 0.2–0.5 g underwent pretreatment in a muffle furnace at 250 °C for 3 h to remove organic matter. Subsequently, the samples were treated with 20 ml of 10% H_2O_2 followed by the addition of 10 ml of 10% HCl to remove authigenic carbonates. To facilitate dispersion, 10 ml of 0.05 mol l^{-1} $(NaPO_3)_6$ was added. The grain size distribution was determined using a Microtrac S3500 particle analyzer at Zhejiang Normal University, which had a detection range from 0.02 μm to 2000 μm.

3.3. Mathematical analysis

The grain size standard deviation method, originally proposed by Boulay et al. (2003) is commonly used to interpret sedimentary environments. This method relies on the variation in the standard deviation of different grain sizes to derive environmentally sensitive factors. It calculates the standard deviation for each grain size in columnar sediments.

EM analysis method that provided valuable information about the sorting, transit, and deposition of sediments (Weltje, 1997) and implemented in the AnalySize software designed by Paterson and Heslop (2015), is a statistical approach used to identify and characterize meaningful end-members in grain size distributions. By assuming the presence of 1–10 EMs, the Gen. Weibull distribution function is employed to conduct a nonparametric decomposition of the grain size data in the profile. To determine the optimal number of end-members, various statistical analyses, including linear correlation (R^2), angular deviation, and end-member correlation are performed. Lower values of angular deviation and end-member correlation signify a more optimal fitting outcome, and when the fitted percentages closely align with the measured percentages, the R^2 value tends to approach 1. Numerous pertinent studies have delved into and employed the EM analysis method, particularly in the context of loess investigations (Jia et al., 2018; Jia et al., 2022; Vriend et al., 2011). In these research endeavors, several scholars have adeptly utilized these models to isolate the dust sources within the loess deposits.

Wavelet analysis is a powerful tool for examining periodic characteristics of signals at different continuous time scales (Morlet, 1982). It is widely used in analyzing periodic changes in climate factors. In this study, the years corresponding to each end-member element were interpolated based on the granularity of end-element decomposition, with an interpolation interval of 50 years. Subsequently, the data were smoothed, and a wavelet analysis package (Grinsted et al., 2004) was conducted using the MATLAB R2016a software (The MathWorks Ltd., USA). Due to climatic disparities, the sedimentary environment differs

between the last deglaciation and the Holocene. Consequently, we performed distinct wavelet analyses on the individual end-members within these two temporal segments. These analyses aimed to identify periodic changes and patterns in the data.

4. Results

4.1. Grain size composition and parameter characteristics

The variation in the grain size composition of ash in the HY2014 profile is visually depicted in Fig. 2. The clay fraction (<4 μm) ranged from 3.04% to 23.15%, with an average of 11.82%, exhibiting a decreasing trend with increasing depth. The silt particles (4–63 μm) dominated the profile varied between 69.81% and 92.55%, with a mean value of 83.22%. The sand fraction (>63 μm) ranged from 0 to 18.66%, with an average of 4.89%, and showed an increasing trend with depth. The median grain size (Md) had an average value of 17.94 μm, ranging from 11.33 μm to 39.93 μm. The mean grain size (Mz) ranged from 14.99 μm to 40.27 μm, with an average of 20.77 μm. The skewness (Sk) varied from 0.07 to 0.61, with an average of 0.38. Notably, the grain size of ash characteristics above 356 cm differed significantly from those below 365 cm. Generally, in the depth range of 3–356 cm, the Mz and Md values exhibited minor fluctuations around the mean value; while above 356 cm, the ash particles gradually became coarser with increasing depth in the profile.

4.2. Curves of grain size frequency distribution and cumulative frequency

The grain size distribution frequency curves of the HY2014 profile were generated by calculating the average grain size content in each stratigraphic layer. At the depth ranging from 3 cm to 390 cm, the curves exhibited a broad peak between 5 μm and 9 μm, with a secondary peak observed in the range of 15–40 μm. Conversely, at depths between 389 cm and 450 cm, the curves displayed a single-peak pattern, with the majority of grain sizes concentrated in the 5 μm to 70 μm range, and a prominent peak around 37 μm.

The probability cumulative curve is a useful mathematical tool for assessing the hydrodynamic conditions of sediments. It provides insights into the various modes of sediment transport, including rolling, jumping, and suspension. The probability accumulation curves of ash in the HY2014 profile exhibited two distinct sections: the jumping component

and the suspension component. The inflection points, which marked the transition between these two components, were primarily observed in the range of 5–6 Φ. The proportion of suspended particles in the profile ranged from 50% to 70% within the depths range of 3–390 cm, whereas the proportion of suspended particles at depths of 391–450 cm decreased to 30–50%.

4.3. Results of grain size standard deviation and EM analysis

Three prominent peaks in standard deviations were observed at 6.00 μm, 15.56 μm, and 40.35 μm (Fig. 5). Based on the variation in standard deviation, the grain size distribution in the sediments can be divided into three components: component 1 (<10.09 μm), component 2 (10.09–23.99 μm), and component 3 (>23.99 μm). Among these components, component 3 exhibits the highest standard deviation and the greatest sensitivity, indicating its significance as the primary dynamic mechanism influencing the characteristics of ash in the profile.

The grain size data were analyzed and decomposed using the AnalySize software. The coefficient of determination (R^2) and average angular deviation (θ) were calculated to determine the optimal number of EMs required for reliable statistical interpretation (Paterson and Heslop, 2015). As shown in Fig. 6A and B, the three EM models demonstrate a satisfactory fit, with relatively high R^2 values. EM1 exhibits three distinct peaks, 7.13 μm, 16.96 μm, and 95.97 μm (Fig. 6C). EM2 and EM3 display single peaks at 28.53 μm and 44 μm, respectively (Fig. 6C). The proportions of EM1 range from 0% to 81.80% (with the average value of 48.49%) and show relatively low values between 14,000 and 10,764 cal yr BP (Fig. 10A). EM2 proportions range from 4.01% to 98.00% (average 38.69%) (Fig. 10C), while EM3 proportions vary from 0% to 71.13% (average 12.81%), with a relatively high value during 14,000 and 10,764 cal yr BP (Fig. 10D).

4.4. Wavelet analysis for each EM

Wavelet analysis was conducted on the curves during the late deglaciation and the Holocene for each end member. Since the late deglaciation, EM1 exhibited a periodic signal of 500–1200 yr, with a relatively weak signal during the 9000–7000 cal yr BP stage (Fig. 7A). Throughout the 14,000-years period, EM2 consistently displayed a 1000 yr scale signal (Fig. 7B). Between 13,000–9000 cal yr BP and 7000–6000 cal yr BP, clear periodic signals of approximately 500 yr
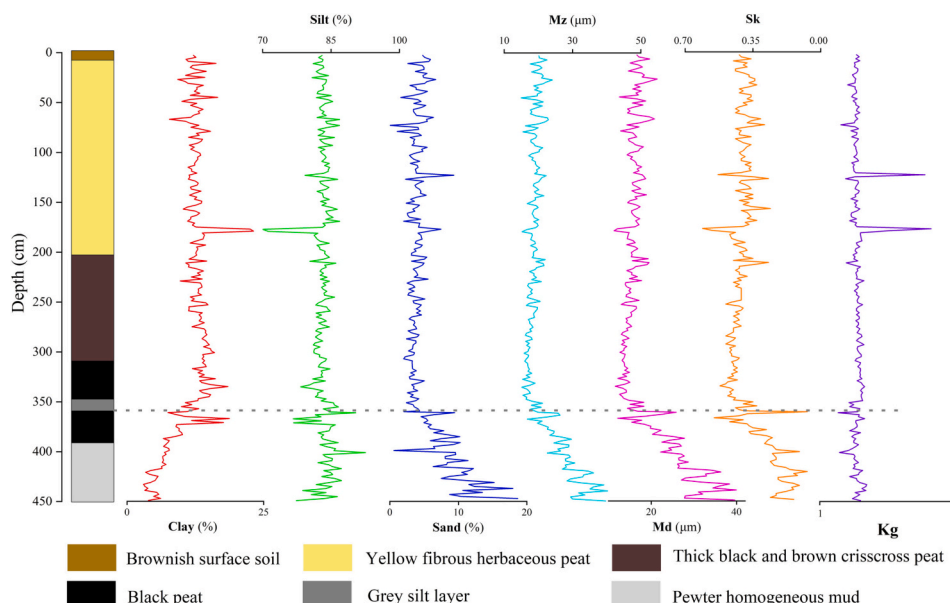
Fig. 2. Variations of grain size parameters in ash along depth in the HY2014 profile.

were observed. During the Holocene, EM2 exhibited a period of 500–1000 yr, with a period of 350–550 yr since 8000 cal yr BP, albeit with a weak intensity during the 5500–4500 cal yr BP stage. A cycle of 220–256 yr was observed during 6500–5500 cal yr BP (Fig. 7E). The EM3 component displayed a periodic signal of 400–600 yr during late deglaciation (Fig. 7C). During the Holocene, EM3 exhibited periodic signals of 2000 yr and 1500 yr, as well as periodic signals of 400–700 yr at 10,000–9000 cal yr BP and after 4000 cal yr BP (Fig. 7F).

5. Discussion

5.1. Provenance of ash and sedimentary environment in the Hongyuan region derived from HY2014 peat archive

The mean grain size of peat sediments in the HY2014 profile ranged from 14.99 μm to 40.27 μm (Fig. 2), which significantly differs from that of the fluvial sediments (30 μm to 300 μm) (Fig. 8A). However, it is comparable to the mean grain size of 16.29 μm to 18.58 μm observed in typical aeolian loess (Wang et al., 2020) (Fig. 8A). Particles ranging from 10 μm to 50 μm are easily transported by winds and constitute the major component of loess, comprising 50–60% of the Malan loess in the Loess Plateau (Liu, 1985) (Fig. 8B). On the other hand, sand (>63 μm) can only be transported through short-term suspension or creep (Wang et al., 2020). The average content of particles ranging from 10 μm to 50 μm was 59.01% (Fig. 8B), whereas the sand content in the sediments of the HY2014 profile ranged from 0% to 18.66%, with an average value of 4.89%.

Both the grain size frequency accumulation curve and cumulative frequency curve serve as crucial indicators for classifying various sediment types (Wang et al., 2020). The grain size frequency distribution curves of the ash at a depth of 3–389 cm in the HY2014 profile, displayed a bimodal distribution (Fig. 3), resembling those found in aeolian loess (Sun et al., 2008). According to the grain size distribution characteristics observed in Chinese loess, the primary peak (around 16–32 μm) represents coarse-grained material transported by the low-level monsoonal circulation, while the secondary peak (2–8 μm) potentially indicates distant dust transported aloft by mid-latitude WWs (Sun et al., 2008). Furthermore, the cumulative frequency curves of the profile exhibited either a single- or two-segment pattern (Fig. 4). The contents of <4 Φ and >11 Φ were both scarce, accounting for <2%. This suggests that the transport process for the peat deposits in the HY2014 profile was relatively simple.

Zhang et al. (2008) developed an empirical discriminant formula for identifying the depositional environment using grain size parameters, which is as follows:

$$F = 20.363Mz - 56.371Sd - 67.922Sk + 23.516Kg - 55.626 \quad (1)$$
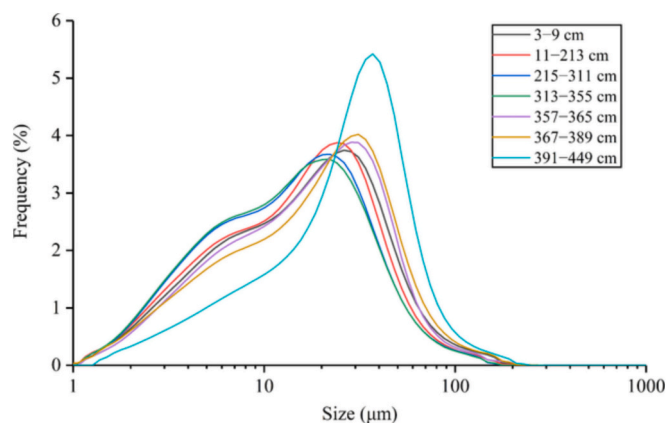
Fig. 3. The grain size frequency distribution curves of each layer in the HY2014 profile.

Where *Mz* represents the mean grain size, *Sd* denotes the standard deviation, *Kg* refers to the kurtosis, and if $F > 0$, it indicates a stable lacustrine sediment; if $F < 0$, it suggests an aeolian sediment.

Based on the grain size parameters of peat sediments from the HY2014 profile, the equation yields $F < 0$. This finding indicates that the ash in the HY2014 profile corresponds to aeolian sediments, thereby providing further support for our perspective on the sources of dust. Many previous studies support our findings. Sun et al. (2001) reported the discovery of the striated mud structure in the Hongyuan peat. These structures indicate sedimentation in a stable environment with weak hydrodynamic forces. The presence of striated mud suggests that water flow had minimal influence on peat deposition. Additionally, Yu and Liu (2010) investigated the surface texture and mineral composition of particles in Hongyuan peat. The results revealed that the minerals were predominantly Quartz and Orthoclase, and the surface texture of Quartz particles exhibited similarities to those found in aeolian deposits (Yu and Liu, 2010).

We collected, measured, and analyzed the grain size of ash from sediments in the Hongyuan peat HY2014 profile spanning the past 14,000 years. In order to confirm the aeolian origin of the ash in HY2014 sediments, we first explored classical empirical formulae and mathematical analysis methods to further investigate the grain size composition characteristics of the ash. Our findings not only verified the origin of the ash in Hongyuan peat but also expanded our understanding of aeolian sediments in the eastern QTP. Based on the grain size characteristics and frequency curves, it was determined that the peat ash in the HY2014 profile originated from aeolian deposition. However, unlike loess sediments, the pedogenesis component (<2 μm) in the HY2014 profile did not unlike a significant proportion of the peat sediments. This can be attributed primarily to the unique sedimentary environment of peatlands.

The changes observed in the frequency distribution curves of samples from the HY2014 profile, transitioning from a bimodal to a single-peak pattern, along with other characteristics, provide insights into the variation of the sedimentary environment (Figs. 2, 3). Particularly, the frequency distribution curves at depths of 391–450 cm exhibit a narrower peak and better sorting (Fig. 3), suggesting a more stable sedimentary environment in that interval. Additionally, within this range, the profile displays a pewter homogeneous mud texture with a notably low organic material content. Furthermore, both the mean grain size (Fig. 9A) and the content of particles >63 μm (Fig. 9B) show a significant increase with depth in the HY2014 profile, indicating enhanced sediment transport capacity. Moreover, the total organic carbon (TOC) content probably indicates variation in the depositional environment. The TOC content of peat in China integrates the preservation and decomposition of organic matter, and its content is influenced by both the type of peat-producing plants and microbial activities (Zeng et al., 2017).

Variations in ash content within a peat profile are influenced by the changing rates of atmospheric dust deposition, as well as differences in peat decomposition and humification over time (Zaccone et al., 2012). The ash content exhibited an inverse correlation with the content of total organic carbon (TOC). As shown in Fig. 9C, the ash content ranged from 9.39% to 93.17%, with an average value of 37.18%, and was significantly higher at the depth of 391–450 cm. In contrast, Zeng et al. (2017) reported that TOC reached its lowest value at the same depth interval in the HY2014 profile. The low values of TOC during this stage indicate reduced bioproductivity and biomass, resulting in minimal organic matter accumulated. Meanwhile, the C/N ratio of the HY2014 profile was significantly low during this period, indicating a higher abundance of aquatic plants compared to other periods (Zeng et al., 2017). Additionally, the pollen content of broadleaved trees and shrubs disappeared during the interval of 12,400–11,500 cal yr BP (Zhou et al., 2010). This sudden change in pollen abundance corresponded to a sharp transition from silty clay to peat and a reversal of radiocarbon dates, potentially indicating a sedimentary hiatus. This stage was characterized by a
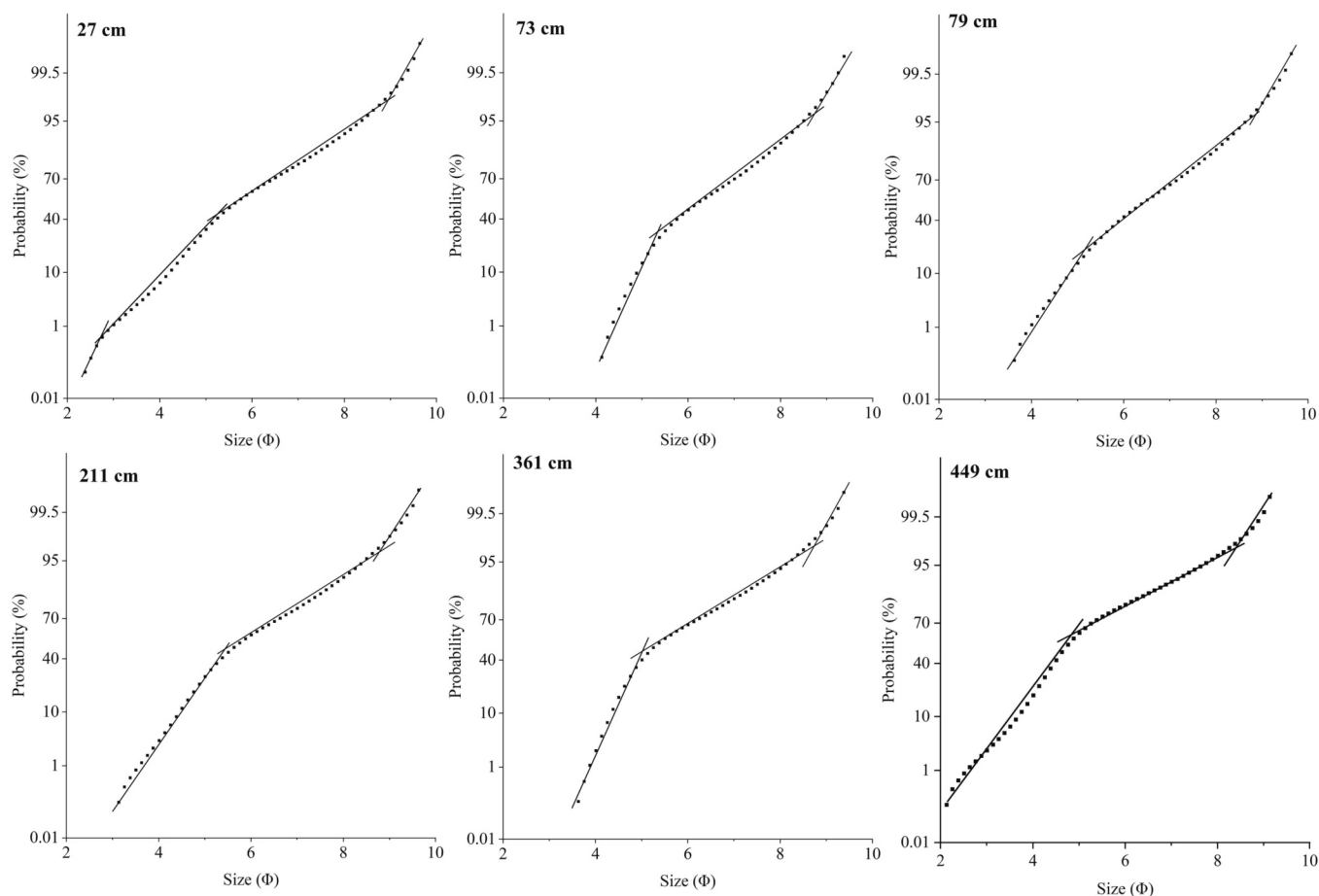
Fig. 4. The probability cumulative curves of typical samples in the HY2014 profile.
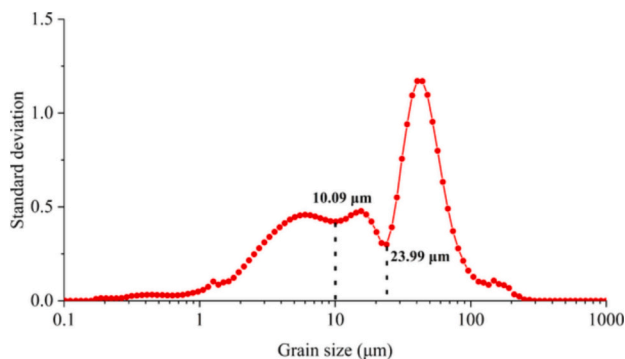
Fig. 5. Standard deviation diagram of grain size in ash in the HY2014 profile.

lacustrine environment in this basin, under cold and wet conditions (Zhou et al., 2010). The vegetation coverage was relatively low in the QTP and its surrounding areas during this period, with extensive areas of loose ice-water sediments exposed on the surface. These exposed sediments served as material sources for the deposition of aeolian dust. Despite a decrease in sediment volume replenishment through floods during the Younger Dryas (YD) event, the presence of strong winds on the QTP facilitated the transport of large quantities of loose sediments, which ultimately accumulated in swampy wetland areas (Huang, 2021). As a result, the sedimentary deposits from this period exhibited higher grain size values.

5.2. Implications for the environmental significance of the three obtained EMs in ash from the HY2014 profile

Based on the analysis of the three modal grain sizes (~7.13, 16.96, and 95.97 μm), EM1 (Fig. 10A) was highly correlated with component 1, representing particles <10.09 μm (Fig. 10B). Previous studies on loess deposits in the QTP suggested that the content of particles in the range of 2–10 μm was mainly transported by high-altitude WWs, while the coarser grain sizes were attributed to sandstorms generated by low-altitude northwesterly wind (Prins and Vriend, 2007). The main source area of these sediments was considered to be the western QTP (Wang and Pan, 1997). Furthermore, satellite remote sensing research indicated that the QTP experiences strong winds, particularly in winter and spring, which easily uplifted dust carried by WWs, resulting in frequent occurrence of sand and dust storms (Fang et al., 2004). This suggests that the coarse-grained sediments with a peak size of 95.97 μm (varying from 62.23 μm to 161.4 μm) were not solely transported over long distances by WWs under normal conditions but were more likely deposited during periods of strong winds and even dust storms (Fig. 6C). Previous studies have also identified similar EMs with multiple peaks, as demonstrated by He et al. (2016) who examined sediments from Ling-geCo Lake in the central QTP. He et al. (2016) found an EM with three peaks at 3–6, 20–40, and 100–250 μm, which were considered indicators of WWs. In summary, EM1 is inferred to be composed of sediments transported by WWs, including materials from both distant and nearby sources, as well as deposits resulting from strong dust storms influenced by WWs.

The EM2 component exhibited a modal size of 28.53 μm (Fig. 10C). The formation of aeolian sediments is influenced by various factors, including the availability of dust sources, wind transport, and favorable
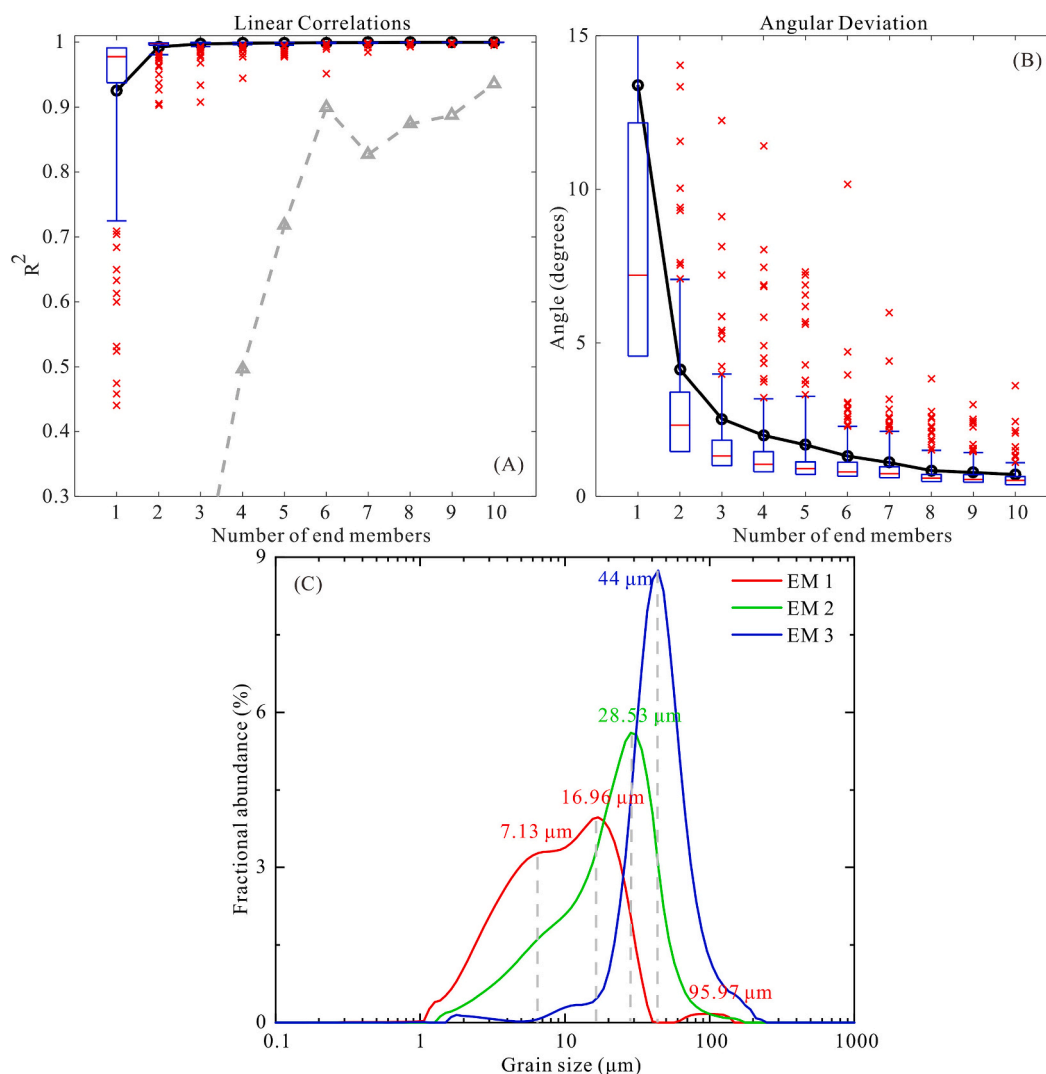
Fig. 6. End-member modeling results for the HY2014 profile. (A) Coefficients of determination (R^2). (B) Angular differences (in degrees) between the reconstructed and observed data sets as a function of the number of end-members (EMs). (C) Grain size distributions of the three Ems.

conditions for dust deposition (Pye, 1995). A study conducted in the northern region of China affected by the ASM, has shown that during years of intensified ASM, the frequency of dust aerosols is significantly lower compared to weak monsoon years (Bai et al., 2020). In the northeastern QTP, the accumulation of aeolian sand and loess is considered an indicator of relatively dry conditions that facilitate sufficient dust supply (Chen et al., 2016; Lu et al., 2011). Based on investigations of aeolian activities in the middle reaches of the Yarlung Zangbo River, it has been observed that a weakening of the ASM and a decrease in summer precipitation extend the period of wind erosion and lead to the degradation of vegetation cover, which promotes the accumulation of wind erosion materials and dust (Li et al., 2020). There have been several periods of increased dust deposition in the region at 8500–7800, 6400–5800, 4500–4000, 3100–1800, and 900 cal yr BP, which aligns with regional low rainfall events and weak ISM events (Li et al., 2020). Multiple indicators revealed degradation of peatland, the retreat of coniferous forest, and a tendency towards a dry and cold climate during the periods of approximately 4500, 4000–3600, 3100–2700, 1400–1200, and 800–600 cal yr BP in the Zoige Basin (Sun et al., 2017). Correspondingly, during these periods, the values of EM2 also tended to be high, suggesting a response to weakened monsoon events. The strengthening of the ASM reduced the supply of sand and dust, which is not conducive to dust transportation. Therefore, we

deduce that EM2 serves as an indicator of the ASM, including the ISM, EASM, and regional plateau monsoons controlled by the ISM. A high value of EM2 indicates a weakening ASM, while a low value of EM2 indicates a strengthened ASM.

The coarsest component, EM3 (Fig. 10D), exhibited a modal size of 44 μm, corresponding to the sensitive component 3 (particles >23.99 μm) (Fig. 10E). EM3 displayed the highest peak and the narrowest peak area, suggesting a source closest to the study area (Sun et al., 2008). EM3 exhibited a similar trend to the sand fraction (>63 μm) (Fig. 10F), mean grain size (Fig. 10G), and ash content. In the QTP, the strengthening of the AWM leads to the transportation of coarse-grained materials from nearby areas to the peatlands, resulting in an increased content of coarse-grained particles. Consequently, particles >40 μm in the ash of the Gonghe peat were considered indicative of the AWM strength (Liu et al., 2014). A study on Quaternary loess in the QTP isolated an EM with a peak grain size of 44 μm, which was interpreted as the product of short-distance suspension, while another EM with a peak grain size of 74 μm was associated with the enhanced AWM (Vriend et al., 2011). Therefore, EM3 can be served as an indicator of the AWM, and its content reflects variations in AWM strength.

The accumulation of ash in Hongyuan peat is a complex process influenced by various transportation forces. The utilization of EMs, which have a strong theoretical foundation and have been widely
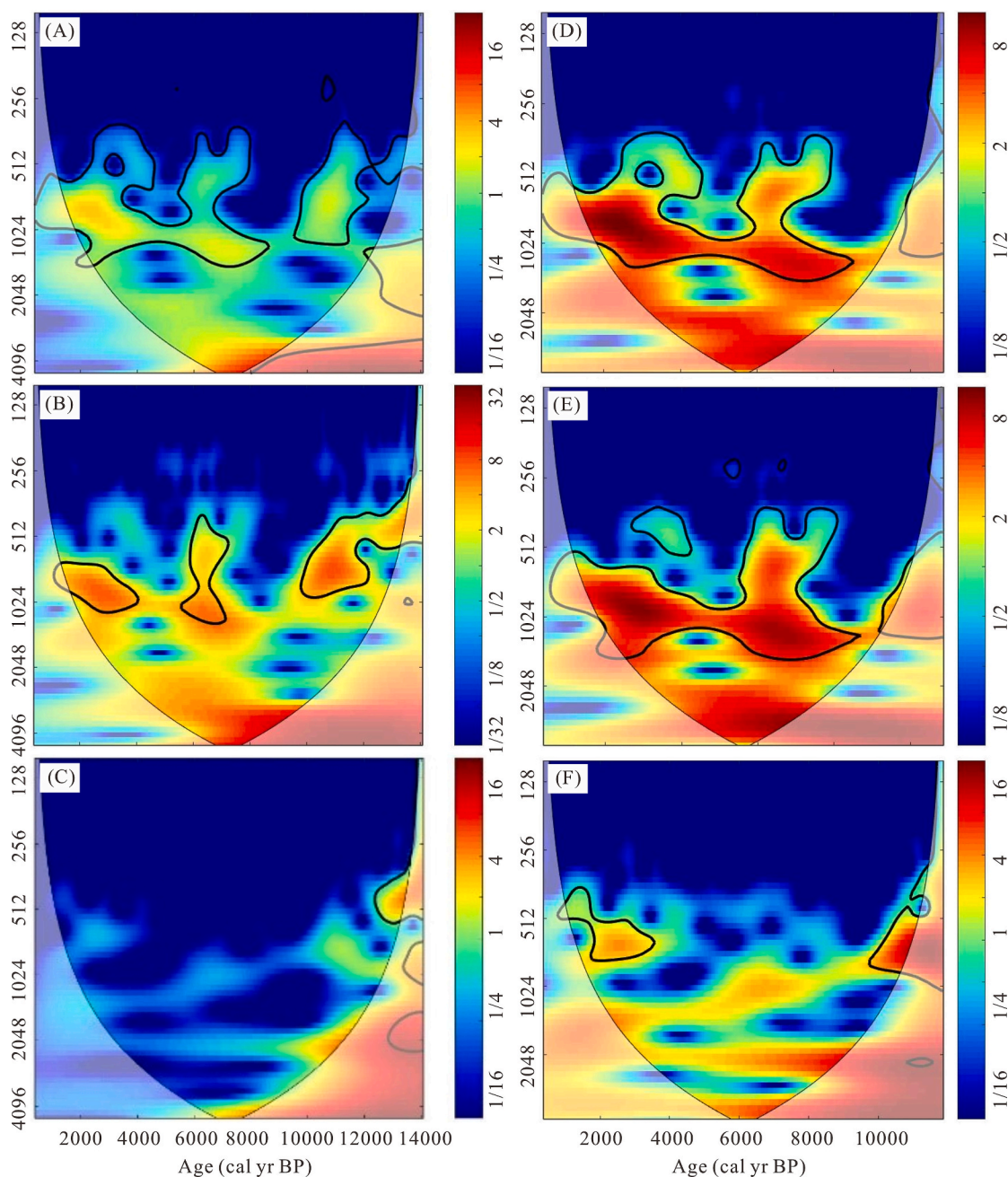
Fig. 7. Wavelet transform of end-member (EM) components of Hongyuan peat ash. (A) EM1, (B) EM2, and (C) EM3 during late deglaciation; and (D) EM1, (E) EM2, and (F) EM3 during the Holocene.

applied in previous studies (He et al., 2016; Jia et al., 2018; Jia et al., 2022), can provide valuable insights into dust accumulation and transport dynamics in the eastern region of the QTP. Due to the distinctive local climate and topographic conditions of Hongyuan peat, the EM representing pedogenesis components is absent. In summary, the EM1 component indicates dust carried by the WWs, and its poor sorting reflects the mixing process during long-distance transportation; the EM2 component reflects the intensity of the ASM, with a lower content indicating a stronger ASM; the EM3 component is likely the result of accumulation driven by the force of the AWM.

5.3. Palaeoclimate reconstruction in the Zoige wetland based on grain size records

The late deglaciation-Holocene aeolian ash preserved in the HY2014

profile provides valuable insights for palaeoclimate reconstruction. Drawing upon our findings and in conjunction with other palaeoclimate archives (Fig. 11), we have identified four distinct periods of palaeoclimate evolution, as outlined below.

5.3.1. Late deglacial period (14,082–11,712 cal yr BP)

During this period, the mean values of EM2 content were the lowest, while the Mz, >63 μm content (%), and EM3 (%) in the HY2014 profile exhibited the highest mean values, revealing a dominance of the AWM in the study area. This is consistent with other proxy reconstructions for the eastern QTP. For example, the TOC content from the HY2014 profile (Zeng et al., 2017) revealed a weakened ASM (Fig. 11B), which is consistent with the $\delta^{18}O$ (carb VPDB) record from the Dongge Cave stalagmite (Carolyn et al., 2005) (Fig. 11C). Therefore, it is inferred that the climate in the study area experienced cold and dry conditions during
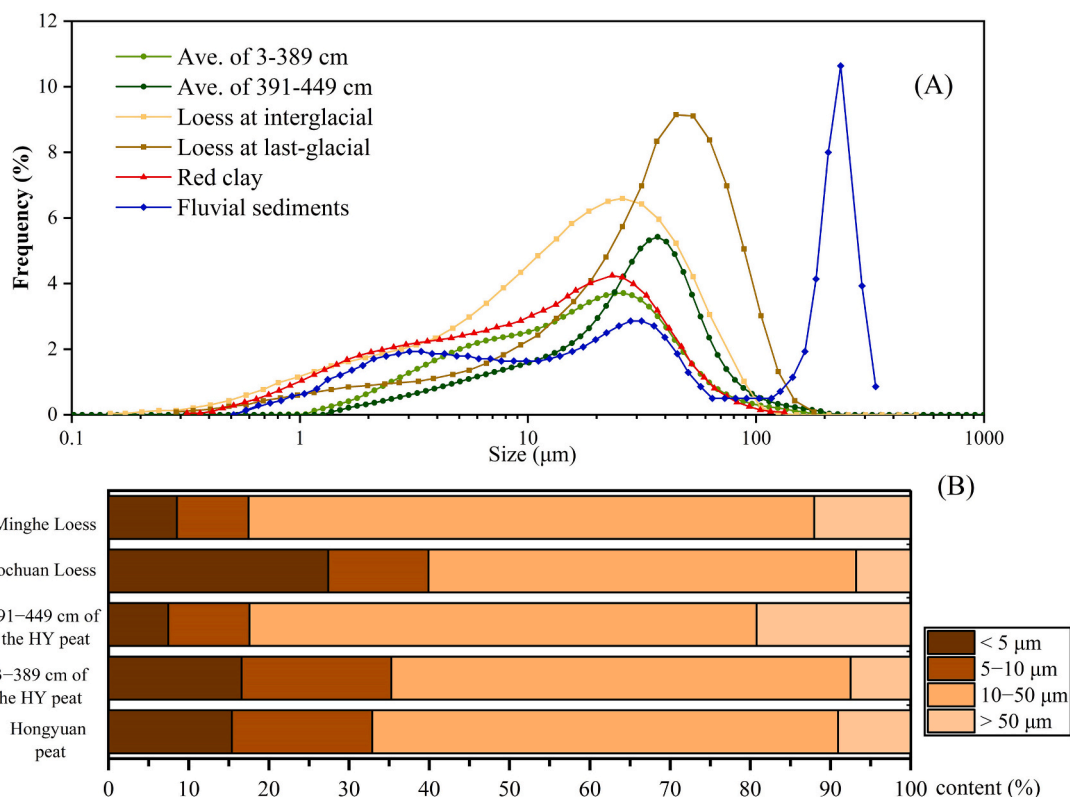
Fig. 8. (A) Comparison of grain size distribution frequency curves of ash in HY2014 profile, aeolian loess from Luochuan profile (Vandenberghe, 2013), red clay and fluvial sediments from Pannonian Basin (Kovacs, 2008). (B) Comparison of grain size composition in different profiles: Minghe Loess and Luochuan Loess in Loess Plateau (Liu, 1985), the average of the 391–449 cm、3–389 cm、3–449 cm in ash of HY2014 profile. (For interpretation of the references to colour in this figure legend, the reader is referred to the web version of this article.)
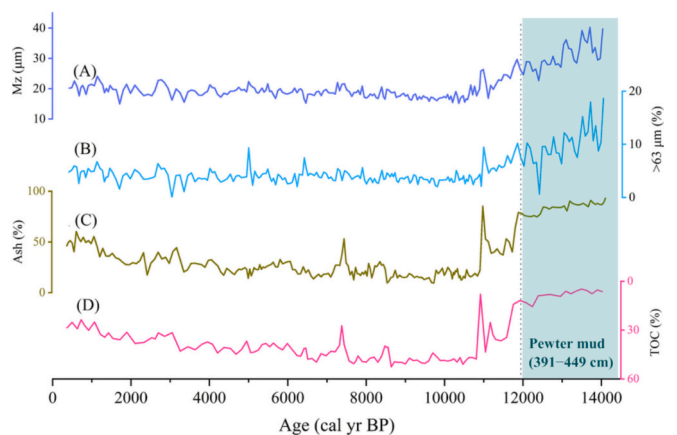
Fig. 9. Variations of the Mz (A), percentage of >63 μm (B), ash content (C), and TOC (Zeng et al., 2017) (D) along depths in the HY2014 profile.

this period under the influence of a strong AWM. Additionally, a mean annual temperature (Le Roux et al., 2012) reconstruction based on brGDGT in the Hongyuan peat showed that the MAT for this period averaged −9.13 °C, lower than the mean temperature (−5.95 °C) (Yan et al., 2021) (Fig. 11D).

EM1, which is considered to represent the intensity of WWs, exhibited low values during this interval, which appears to be inconsistent with the predominance of WWs during the late deglacial period as suggested by previous studies (An et al., 2012; Jia et al., 2022). Theoretically, the climate was warm and humid during the period of 15,700–12,900 cal yr BP (Bølling-Allerød, BA) (López-Avilés et al., 2022). However, the relatively coarse grain size seems to contradict the
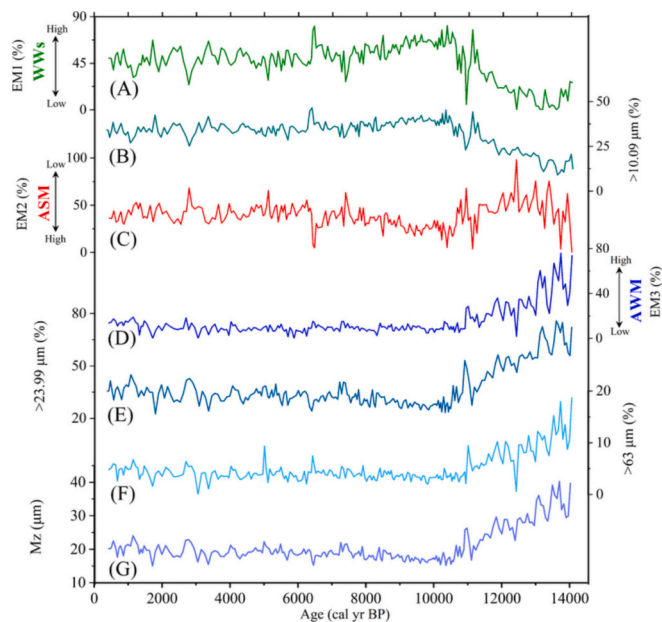
Fig. 10. Changes in (A) the content of EM1, (B) the content of the sensitive component (<10.09 μm) using the Deviation method, (C) the content of EM2, (D) the content of EM3, (E) the content of the sensitive component (>23.99 μm) using the Deviation method, (F) the particle content (>63 μm), (G) the mean grain size of the HY2014 profile.
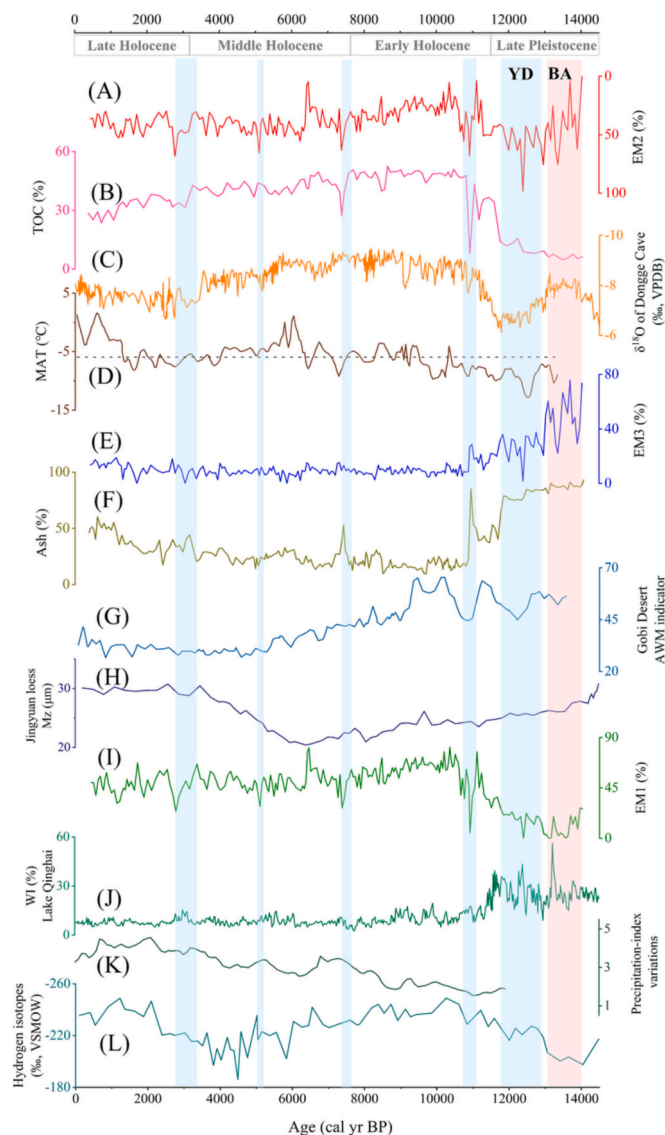
Fig. 11. Comparison among the (A) EM2 percentage content and (B) TOC of the HY2014 profile (Zeng et al., 2017); (C) δ¹⁸O (carb VPDB) from Dongge Cave (Carolyn et al., 2005); (D) mean annual temperature obtained from brGDGTs in Hongyuan peat (Yan et al., 2021); (E) EM3 percentage content and (F) the ash content in the HY2014 profile; (G) the AWM indicator from Gobi Desert (the 20–200 μm component for the Huangyanghe section) (Li and Morrill, 2015); (H) the mean grain size of Jingyuan loess (Sun et al., 2010); (I) EM1 percentage content in HY2014 profile; (J) westerlies index obtained from Lake Qinghai sediments (WI, flux of >25 μm fraction) (An et al., 2012); (K) precipitation-index variations in low-elevation regions (Zhang and Feng, 2018); (L) the hydrogen isotope results of the fatty acids from Jiang Co, northwest China (Xie, 2019). Note: the orange box indicates warm climate, and the blue box indicates cold climate. (For interpretation of the references to colour in this figure legend, the reader is referred to the web version of this article.)

warm and humid climatic conditions during this period of 14,082–12,106 cal yr BP at a depth of 450–392 cm. In fact, during this period, the mountain glaciers extensively melted in the upper reaches of the Zoige Basin, resulting in massive floods (13,600 ± 1200–13,000 ± 1100 cal yr BP) in the mainstream of the Yellow River and the Zoige Basin (Huang, 2021). Moreover, the repeated melting and erosion of Quaternary glaciers generated a large amount of detrital material (Zhao et al., 2006). These sediments carried by the floods would be deposited at suitable locations along the banks of rivers and lakes under high water and stagnant flow conditions. Consequently, abundant sediments

carried by the rivers were deposited in the Hongyuan peatlands. Therefore, it is not surprising that the grain size was relatively high during this period.

In general, the late-deglacial palaeoclimate in the region can be characterized as cold and dry, although there were still a series of climate fluctuations. Based on the variability observed among the EMs, the HY2014 profile indicated that the YD event ended at 11,712 cal yr BP, which is consistent with the end of a local YD event suggested by δ¹⁸O records from Lake Kuhai at 11,600 cal yr BP (Yan et al., 2018). Additionally, pollen records from Tianchi Crater Lake in NE China indicated the end of the YD event at 11,700 cal yr BP (Liu et al., 2023). This consistency suggests that the conclusion regarding the end of the YD event in the Hongyuan peatland is consistent with findings from other regions. During the YD event, the Yellow River experienced river capture and cut through the ancient Zoige Lake (Wang et al., 1995), resulting in the transport of a large area of bare loose sediments to the peatland by strong plateau winds (Huang, 2021). Therefore, the grain size was high and roughly equivalent to that of the warm BA period.

5.3.2. Early Holocene (11,712–7634 cal yr BP)

After ~11,700 cal yr BP, there was an increase in the contents of TOC and EM1 (Fig. 11), while there was a decline in ash, EM2, and EM3 (Fig. 11), indicating a shift towards a warm and wet climate. However, there was an abrupt increase in ash and EM2 (Fig. 11A) during the interval of 11,090–10,938 cal yr BP, which may correspond to the 11,100 cal yr BP cold event observed in the North Atlantic ice floes (Bond et al., 1997). This event was also recorded by the low TOC in the HY2014 profile (Zeng et al., 2017) (Fig. 11B).

Following this cold event, the subsequent decrease in EM2 and increase in TOC suggested an enhanced ASM during that period. Stalagmite δ¹⁸O records from Chongqing, southwest China, indicated relatively stable and strong EASM during 8000–6000 yr BP, with the strongest monsoon occurring during 8000–7000 yr BP (Yang et al., 2019). Loess deposits from the Luoyang Basin also indicated a strong EASM and a warm and wet climate between 11,500–8500 cal yr BP (Jia et al., 2021). Additionally, stalagmite δ¹⁸O records from Dongge Cave (Carolyn et al., 2005) (Fig. 11C) and Sanbao Cave (Cheng et al., 2016) also indicated a stronger ASM and increased precipitation during the Early Holocene.

As the ASM strengthened, there was a gradual weakening of the AWM. Grain size analysis of loess from the Loess Plateau indicated a continuous weakening of the AWM during 11,700–6500 cal yr BP, likely associated with the ongoing reduction in ice cap volume in the northern region (Kang et al., 2020). The 20–200 μm component at the Huangyanghe section, selected as an indicator of the AWM in the Gobi Desert, suggested a weakening trend of the AWM during the Early Holocene (Li and Morrill, 2015) (Fig. 11G). The AWM in Zoige wetland gradually retreated in an oscillating manner from 11,500 to 8200 cal yr BP (Yu et al., 2011).

The fluctuations in EM1 and the component content <10.09 μm indicate the presence of strong WWs during the early Holocene. However, this finding contradicts the results of An et al. (2012) who reported a weakening of WWs based on the Qinghai Lake sediment records (Fig. 11J). Modern observations suggest that the westerlies are the primary source of precipitation in Central Asia (Karger et al., 2017); therefore, precipitation on the windward slopes influenced by WWs can reflect their strength in Central Asia. The development of local precipitation indices, based on the pollen synthesis from five low-altitude peaks in the Altai Mountains, suggests a general trend of increasing WWs during the early Holocene (Zhang and Feng, 2018) (Fig. 11K). In summary, the early Holocene transitioned from cold-dry to warm-wet, characterized by the intensification of WWs and the EASM.

5.3.3. Middle Holocene (7634–3100 cal yr BP)

Around 7634 cal yr BP, there was a notable decrease in TOC was observed, while ash, EM2, and EM3 exhibited rapid increases,

suggesting a weakening of the EASM and a strengthening of the AWM. Concurrently, the brGDGT records in the Hongyuan peat indicated a significant decline in MAT from −4.89 °C to −9.21 °C, occurring in <400 years (Yan et al., 2021). Therefore, we refer to this cold period as the end of the warm early Holocene. This cold event was also observed in the Lake Ximencuo between 7900 and 7400 cal yr BP, characterized by a distinct minimum in TOC content and a decrease in $\delta^{13}C$ values (Mischke and Zhang, 2010). Following this cold event, the values of EM2 (Fig. 11A) and TOC (Fig. 11B) increased, indicating a strengthening of the ASM. At 6000 cal yr BP, the maximum local MAT (Yan et al., 2021) (Fig. 11D) suggested a warm climate in the local area. The end of the "Holocene Optimum" warm phase occurred at ~4200 cal yr BP (Li et al., 2017). Around this time, the content of EM2 and EM3 increased, while TOC decreased, indicating a temporary enhancement of the AWM and a decrease in the ASM. The 8200 and 4200 cal yr BP events are considered the two most significant cold events of the Holocene; however, in the study region, the 7400 cal yr BP cold event had a more pronounced and significant impact.

The EM1 (Fig. 11I) component in the middle Holocene was slightly lower than in the early Holocene, but overall, the WWs remained strong. The precipitation index from the Tianshan Mountains showed a continued strengthening of WWs during this period (Zhang and Feng, 2018) (Fig. 11K). Results from lacustrine deposits in Jiangcuo Lake in the central QTP, using the TRACE21 climate model to simulate changes in the intensity since the Holocene, indicated a sharp increase in WWs intensity since 6000 cal yr BP, with the southern boundary of the WWs gradually expanding southward (Xie, 2019) (Fig. 11L).

5.3.4. Late Holocene (3100–0 cal yr BP)

A further increase in ash content in the HY2014 profile was accompanied by a significant increase in EM2 and EM3, indicating a cold event characterized by a weakened ASM around 3100 cal yr BP (Fig. 11). Similar cold events were observed in other regions as well. The Loess Plateau, for instance, indicates a large-scale cooling event at 3100 cal yr BP, marking the end of the warm and wet middle Holocene and transitioning to a dry and cold climate (Jia et al., 2021). Changes in precipitation patterns in northern China also suggest a rapid weakening of the summer monsoon from 3300 cal yr BP (Chen et al., 2015).

Following this cold event, all EMs (Fig. 11) exhibited substantial and frequent fluctuations, especially EM 3 (Fig. 11E). During this period, there was a temporary enhancement of the AWM between 1200 and 600 yr BP, as evidenced by a significant increase in EM3 and ash content. Pb depositions from the Badain Jaran Desert and Tengger Deserts also increased between 1700 and 900 yr BP, possibly indicating a strengthened AWM in northern East Asia (Ferrat et al., 2012). In contrast, the WWs and ASM experienced weakening, particularly during 1400–1200 cal yr BP, indicating a clear declining trend. Li et al. (2020) proposed that there was an enhanced aeolian accumulation centered around 900 yr BP in the Yarlung Zangbo River, which aligns with a weak ISM. The northern arid zone of Central Asia also witnessed decreased humidity and weakened WW during this period (Chen et al., 2008). The WWs exhibited variability in intensity, similar to the ASM, with the Qinghai Lake region experiencing weak WWs during this period (An et al., 2012) (Fig. 11J).

The magnitude of atmospheric circulation changes during this phase was notably higher than that in the early and middle Holocene, suggesting a trend towards climate instability during the late Holocene. In addition to climate factors, the influence of human activities gradually increased during this period. For example, the spodumene record from the Gonghe Basin indicates considerable pasture degradation induced by grazing after 1600 yr BP, possibly leading to increased dust emissions into the atmosphere (Huang et al., 2017).

5.4. A new insight on the interaction between the WWs and Asian monsoons

Numerous studies have indicated that variations in the AWM and WWs are influenced by changes in ice volume in the Northern Hemisphere and temperature fluctuations in mid-to-high latitudes on an orbital and sub-orbital scale (Liu et al., 2020). The attenuation of the Atlantic meridional overturning circulation (AMOC) during cold periods in the North Atlantic and Arctic regions can lead to the cooling of extensive areas in the Northern Hemisphere's mid-to-high latitudes, while the intensification of the Mongolian-Siberian High under relatively cold conditions may induce northward airflow. Consequently, the AWM is strengthened (Sun et al., 2012; Wen et al., 2016), and the westerly belt migrates southward to the northeastern QTP (An et al., 2012). The monsoon systems are driven by various mechanisms on a millennial scale, such as solar insolation, ENSO, Hadler circulation, and so on. The HY2014 profile covers nearly 14,000 years, providing a comprehensive record of the controlled mechanisms and interactions of atmospheric circulation at different time scales.

The ISM is primarily influenced by solar insolation (Bird et al., 2017). Palaeoclimate records from the QTP and its surrounding regions showed that the ISM reached its peak during the early and middle Holocene, approximately between 10,000 and 6000 cal yr BP, coinciding with the highest Boreal summer insolation, strong tropical Pacific sea surface temperature gradients (Lu et al., 2000) that resembled a La Niña–like mean state (Bird et al., 2017). However, the trend observed in EM2 does not exactly mirror the changes in solar insolation but rather lags behind them. It seems that besides solar radiation, glacial climate boundary conditions also played a role during this period. It was only after the retreat of ice sheets that insolation became the dominant factor controlling the monsoon dynamics (Carolyn et al., 2005).

EM2 indicates that during the early and middle Holocene, the ASM remained relatively strong. As depicted in Fig. 7, the ASM cycle represented by EM2 has exhibited cycles of 500–1000 yr, 350–550 yr, and 220–256 yr during the Holocene which aligns with similar findings in a previous study (e.g., Xian et al., 2006; Zeng et al., 2017). $\delta^{13}C$ analysis of Hongyuan peat revealed monsoon cycles of 1428, 512, 255, and 217 yr (Xian et al., 2006). The $\delta^{13}C$ and $\delta^{18}O$ records from the Niu Cave demonstrated an 830-year periodicity in the EASM during the late Holocene (Zhao et al., 2016), possibly resulting from long-term changes in tropical SST and its interaction with low-latitude monsoons (Russell et al., 2003). Zhuye Lake, situated on the northwestern edge of the Asian monsoon, also exhibited cycles of 1024, 512, and 256 yr (Li et al., 2012). A comparison between the North Atlantic drift-ice index and Chinese stalagmite isotopic records suggested a potential linkage between weak ASM events and Holocene ice-rafting events in the North Atlantic, with notable weak EASM events (Zhao et al., 2016).

EM3 exhibits cycles of 2000 and 1500 yr since the YD event, with cycles of 400–700 yr during 10,000 to 9000 cal yr BP and after 4000 cal yr BP. Lu et al. (2000) found that intensified AWM events displayed periodicities ranging from 1000 yr to 2770 yr, with a dominant cycle of approximately 1450 yr. The ~1500 yr cycle was also prominent in Greenland ice cores (Mayewski et al., 2004), North Atlantic sediments (Bond et al., 2001), and the northern Yellow Sea of China (Nan et al., 2017), and it is believed to be associated with solar activity. Reduced solar radiation can induce changes in the atmosphere and ocean currents, resulting in a strengthened AWM (Xiao et al., 2006). In addition, variations in the extent of Northern Hemisphere ice cover at high latitudes and changes in atmospheric temperature at middle-to-high latitudes can influence the intensity of the AWM (Kang et al., 2020; Wen et al., 2016). The increased ice volume in the high-latitude Northern Hemisphere enhances the Siberian High and/or displaces it southward through downstream atmospheric cooling in the middle latitudes. This, in turn, further amplifies wind and temperature gradients over East and South Asia, strengthening the AWM (Kang et al., 2020).

EM1 exhibited cycles of 500–1200 yr, with a weak periodic signal

during 9000–7000 cal yr BP. The AMOC plays a significant role in shaping the WWs on a millennium scale. A slowdown in the AMOC triggers a dipole SST anomaly and even substantial cooling in the high-latitude North Atlantic. As a result, temperatures in the high-latitude Northern Hemisphere decreased, leading to a high-pressure anomaly in the middle latitude and a low-pressure anomaly over the pole. This displacement causes the westerlies at 500 hPa to shift northward in the mid-latitudes (Li et al., 2019). Chen et al. (2016) discovered a close correlation between winter insolation and precipitation in the westerly zone, suggesting that winter insolation may have governed precipitation variability in the Holocene westerly zone.

In 14,000–11,900 cal yr BP, the regional AWM exhibited greater intensity, while the ASM and WWs weakened, resulting in cold and dry conditions in the Hongyuan peatland. Following the YD event, the ASM and WWs rapidly strengthened, whereas the AWM strength relatively decreased. From 10,900 cal yr BP to 3300 cal yr BP, the ASM and WWs dominated this region, whereas the AWM strength was noticeably weaker. The region experienced warm and wet except for 8400–8200 cal yr BP, 7700–7400 cal yr BP, 6400–6200 cal yr BP, 5200–5000 cal yr BP, and 4300–4000 cal yr BP, during which the AWM intensified and local temperatures dropped. Between 3300 cal yr BP and 400 cal yr BP, the AWM strength gradually strengthened while the ASM and WWs significantly declined, particularly during the periods of 3300–2800 cal yr BP, 2100–1900 cal yr BP, and 1400–1300 cal yr BP. Overall, when the AWM became stronger, the ASM and WWs exhibited relatively weaker intensity, resulting in a predominantly cold and dry regional climate.

Previous studies have provided evidence for an inverse correlation between the ASM and AWM on a millennial scale (Kang et al., 2020; Wen et al., 2016). The strongest WWs during the Holocene were observed in the middle Holocene (6000–3100 cal yr BP) (Jia et al., 2018), whereas the early Holocene is generally regarded as the phase of the strongest ASM (Jia et al., 2021). Studies conducted on the QTP have demonstrated an approximately inverse correlation between the ASM and WWs during the mid-to-late Holocene (Ning et al., 2022). Furthermore, it has been observed that increased dust emissions over East Asia were associated with the southward movement of WWs during cold climate conditions (An et al., 2012), although the findings of our study differ from these previous findings. Conversely, Li et al. (2021) reported a positive correlation between ASM and regional precipitation changes dominated by WWs on the QTP based on Holocene precipitation records from loess and lake sediments. Based on our comprehensive records of grain size distribution data from peat ash, we propose that in the eastern QTP, WWs exhibit a positive correlation with ASM and demonstrate a nearly synchronous variation trend, while the WWs show an inverse relationship with the AWM.

6. Conclusions

We have utilized detailed grain size analyses of a peat profile in the Hongyuan peatland to reconstruct the atmospheric circulation patterns in the Zoige region since the last deglaciation. The main findings are outlined below:

(1) Through the integration of the EM model, the grain size of ash in the HY2014 profile can be categorized into three distinct end-members. EM1 exhibited a triple peak (7.13 μm, 16.96 μm, and 95.97 μm) corresponding to the WWs. EM2 displayed a diverse grain size of 28.53 μm, indicative of the ASM. EM3 showcased a diverse grain size spectrum at 44 μm, representing the AWM.

(2) Four stages in palaeoclimate evolution were identified: a cold and dry climate predominantly influenced by the AWM during the last deglaciation (14,000–11,712 cal yr BP); transitioning into a warm-wet climate occurred with the AWM weakening while the ASM and WWs strengthening during the early Holocene (11,712–6261 cal yr BP); a warm-wet climate with the dominance of the WWs and ASM and further weakening of the AWM

during the middle Holocene (6261–2800 cal yr BP); and a dry-cold climate after 2800 cal yr BP accompanied by fluctuations in the ASM and WWs, along with an intensification of the AWM.

(3) Throughout the Holocene, the WWs demonstrated a cycle of 500–1200 yr, the ASM exhibited a cycle spanning 500 yr to 1000 yr, and the AWM showed 2000-yr and 1500-yr periodicities. The intensity of each atmospheric circulation system is likely primarily influenced by solar activity.

(4) The disparities among the three end-members indicated a positive correlation between the WWs and the ASM, whereas an inverse relationship was observed between the WWs and the AWM.

Declaration of Competing Interest

The authors declare the following financial interests/personal relationships which may be considered as potential competing interests:

Zeng, Mengxiu reports financial support, article publishing charges, equipment, drugs, or supplies, and statistical analysis were provided by Zhejiang Normal University.

Data availability

Data will be made available on request.

Appendix A. Supplementary data

Supplementary data to this article can be found online at https://doi.org/10.1016/j.palaeo.2023.111814.

References

An, F.Y., Liu, X.J., Zhang, Q.X., Wang, Y.X., Chen, T.Y., Yu, L.P., Lu, B.L., Chang, Q.F., 2018. Drainage geomorphic evolution in response to paleoclimatic changes revealed 12.8 ka in the eastern Kunlun Mountains, NE Qinghai-Tibetan Plateau. Geomorphology 319, 117–132. https://doi.org/10.1016/j.geomorph.2018.07.016.

An, Z.S., Colman, S.M., Zhou, W.J., Li, X.Q., Brown, E.T., Jull, A.J.T., Cai, Y.J., Huang, Y. S., Lu, X.F., Chang, H., Song, Y.G., Sun, Y.B., Xu, H., Liu, W.G., Jin, Z.D., Liu, X.D., Cheng, P., Liu, Y., Ai, L., Li, X.Z., Liu, X.J., Yan, L.B., Shi, Z.G., Wang, X.L., Wu, F., Qiang, X.K., Dong, J.B., Lu, F.Y., Xu, X.W., 2012. Interplay between the Westerlies and asian monsoon recorded in Lake Qinghai sediments since 32 ka. Sci. Rep. 2, 619. https://doi.org/10.1038/srep00619.

Bai, B., Zhang, Q., Shao, W., Wang, Y., Tan, D., 2020. The Response of the Aerosol distribution to Monsoon Intensity over the Summer Monsoon transition Zone. Front. Earth Sci. 7, 356. https://doi.org/10.3389/feart.2019.00356.

Bird, B.W., Lei, Y., Perello, M., Polissar, P.J., Yao, T., Finney, B., Bain, D., Pompeani, D., Thompson, L.G., 2017. Late-Holocene indian summer monsoon variability revealed from a 3300-year-long lake sediment record from Nir'pa Co, southeastern Tibet. The Holocene 27, 541–552. https://doi.org/10.1177/0959683616670220.

Blaauw, M., Christen, J.A., 2011. Flexible paleoclimate age-depth models using an autoregressive gamma process. Bayesian Anal. 6, 457–474. https://doi.org/10.1214/ba/1339616472.

Bond, G., Kromer, B., Beer, J., 2001. Persistent Solar Influence on North Atlantic climate during the Holocene. Science 294, 2130–2136. https://doi.org/10.1126/science.1065680.

Bond, G., Showers, W., Cheseby, M., Lotti, R., Almasi, P., Demenocal, P., Priore, P., Cullen, H., Hajdas, I., Bonani, G., 1997. A Pervasive Millennial-Scale Cycle in North Atlantic Holocene and Glacial Climates. Science 278, 1257–1266. https://doi.org/10.1126/science.278.5341.1257.

Boulay, S., Colin, C., Trentesaux, A., Pluquet, F., Bertaux, J., Blamart, T., Buehring, C., Wang, P., 2003. Mineralogy and Sedimentology of Pleistocene Sediment in the South China Sea (ODP Site 1144). Proc. Ocean Drill. Prog. Sci. Results 184, 1–21. https://doi.org/10.2973/odp.proc.sr.184.211.2003.

Carolyn, A.D., Hai, C., Daoxian, Y., Yanjun, C., Meiliang, Z., Yushi, L., Jiaming, Q., Zhisheng, A., Justin, R., 2005. A high-resolution, absolute-dated Holocene and deglacial Asian monsoon record from Dongge Cave, China. Earth Planet. Sci. Lett. 233, 71–86. https://doi.org/10.1016/j.epsl.2005.01.036.

Chen, F.H., Wu, D., Chen, J.H., Zhou, A.F., Yu, J.Q., Shen, J., Wang, S.M., Huang, X.Z., 2016. Holocene moisture and East asian summer monsoon evolution in the northeastern Tibetan Plateau recorded by Lake Qinghai and its environs: a review of conflicting proxies. Quat. Sci. Rev. 154, 111–129. https://doi.org/10.1016/j.quascirev.2016.10.021.

Chen, F.H., Xu, Q.H., Chen, J.H., Birks, H.J.B., Liu, J.B., Zhang, S.R., Jin, L.Y.Y., An, C.B., Telford, R.J., Cao, X.Y., Wang, Z.L., Zhang, X.J., Selvaraj, K., Lu, H.Y., Li, Y.C., Zheng, Z., Wang, H.P., Zhou, A.F., Dong, G.H., Zhang, J.W., Huang, X.Z., Bloemendal, J., Rao, Z.G., 2015. East asian summer monsoon precipitation variability since the last deglaciation. Sci. Rep. 5, 11186. https://doi.org/10.1038/srep11186.

Chen, F.H., Yu, Z.C., Yang, M.L., Ito, E., Wang, S.M., Madsen, D.B., Huang, X.Z., Zhao, Y., Sato, T., Birks, H.J.B., Boomer, I., Chen, J.H., An, C.B., Wunnemann, B., 2008. Holocene moisture evolution in arid Central Asia and its out-of-phase relationship with asian monsoon history. Quat. Sci. Rev. 27, 351–364. https://doi.org/10.1016/j.quascirev.2007.10.017.

Cheng, H., Edwards, R.L., Sinha, A., Spotl, C., Yi, L., Chen, S.T., Kelly, M., Kathayat, G., Wang, X.F., Li, X.L., Kong, X.G., Wang, Y.J., Ning, Y.F., Zhang, H.W., 2016. The asian monsoon over the past 640,000 years and ice age terminations. Nature 534, 640–646. https://doi.org/10.1038/nature18591.

Fang, X.M., Han, Y.X., Ma, J.H., Song, L.C., Yang, S.L., 2004. Dust storms and loess accumulation on the Tibetan Plateau: a case study of dust event on 4 March 2003 in Lhasa. Chin. Sci. Bull. 1084–1090.

Ferrat, M., Weiss, D.J., Dong, S.F., Large, D.J., Spiro, B., Sun, Y.B., Gallagher, K., 2012. Lead atmospheric deposition rates and isotopic trends in asian dust during the last 9.5 kyr recorded in an ombrotrophic peat bog on the eastern Qinghai-Tibetan Plateau. Geochim. Cosmochim. Acta 82, 4–22. https://doi.org/10.1016/j.gca.2010.10.031.

Grinsted, A., Moore, J., Jevrejeva, S., 2004. Application of Cross Wavelet Transform and Wavelet Coherence to Geophysical Time Series. Nonlinear Process. Geophys. 11, 561–566. https://doi.org/10.5194/npg-11-561-2004.

Harrison, S.P., Kohfeld, K.E., Roelandt, C., Claquin, T., 2001. The role of dust in climate changes today, at the last glacial maximum and in the future. Earth Sci. Rev. 54, 43–80. https://doi.org/10.1016/S0012-8252(01)00041-1.

He, Y., Bao, Z., Hou, J., Brown, E., Wang, M., Xie, S.E.A., 2016. Variation of the mid-latitude westerlies and Indian summer monsoon since the last deglaciation: Evidence from grain-size data from Linggo Co, central Tibet. Chin. Sci. Bull. 61, 3583–3595. https://doi.org/10.1360/N972016-00610.

Huang, C.C., 2021. Palaeoflood deposits in the Zoige Basin and the enlightening on the formation of the Yellow River drainage system on the Tibetan Plateau. Acta Geogr. Sin. 76, 612–625. https://doi.org/10.11821/dlxb202103009 (in Chinese with English abstract).

Huang, X.Z., Liu, S.S., Dong, G.H., Qiang, M.R., Bai, Z.J., Zhao, Y., Chen, F.H., 2017. Early human impacts on vegetation on the northeastern Qinghai-Tibetan Plateau during the middle to late Holocene. Prog. Phys. Geogr. 41, 286–301. https://doi.org/10.1177/0309133317703035.

Jia, J., Liu, H., Gao, F.Y., Xia, D.S., 2018. Variations in in the westerlies in Central Asia since 16 ka recorded by a loess section from the Tien Shan Mountains. Palaeogeogr. Palaeoclimatol. Palaeoecol. 504, 156–161. https://doi.org/10.1016/j.palaeo.2018.05.021.

Jia, Y.N., Zhang, Y.Z., Huang, C.C., Wang, N.L., Qiu, H.J., Wang, H.Y., Xiao, Q.L., Chen, D., Lin, X., Zhu, Y., Fu, L., Gu, K., Patton, H., 2022. Late Pleistocene-Holocene aeolian loess-paleosol sections in the Yellow River source area on the northeast Tibetan Plateau: chronostratigraphy, sediment provenance, and implications for paleoclimate reconstruction. Catena 208, 105777. https://doi.org/10.1016/j.catena.2021.105777.

Jia, Y.N., Zhang, Y.Z., Wang, N.L., Chang, H.C., Qiu, H.J., Wang, H.Y., Yu, Y.K., Seilbike, A., Zou, M.B., Lin, X., Tan, Z.H., Liu, W.Q., Hu, S., Nicholas, R., P., check, 2021. Chronostratigraphic framework and paleoenvironmental interpretation of the Holocene loess-paleosol sequence in the Luoyang Basin, Central China. Aeolian Res. 48, 100657 https://doi.org/10.1016/j.aeolia.2020.100657.

Kang, S.G., Du, J.H., Wang, N., Dong, J.B., Wang, D., Wang, X.L., Qiang, X.K., Song, Y.G., 2020. Early Holocene weakening and mid- to late Holocene strengthening of the East asian winter monsoon. Geology 48, 1043–1047. https://doi.org/10.1130/G47621.1.

Karger, D.N., Conrad, O., Bohner, J., Kawohl, T., Kreft, H., Soria-Auza, R.W., Zimmermann, N.E., Linder, H.P., Kessler, M., 2017. Climatologies at high resolution for the earth's land surface areas. Sci. Data 4, 170122. https://doi.org/10.1038/sdata.2017.122.

Kovacs, J., 2008. Grain-size analysis of the Neogene red clay formation in the Pannonian Basin. Int. J. Earth Sci. 97, 171–178. https://doi.org/10.1007/s00531-006-0150-2.

Le Roux, G., Fagel, N., De Vleeschouwer, F., Krachler, M., Debaille, V., Stille, P., Mattielli, N., Van, D.K.W.O., Van Leeuwen, J.F.N., Shotyk, W., 2012. Volcano- and climate-driven changes in atmospheric dust sources and fluxes since the late Glacial in Central Europe. Geology 40, 335–338. https://doi.org/10.1130/G32586.1.

Li, N.N., Chambers, F.M., Yang, J.X., Jie, D.M., Liu, L.D., Liu, H.Y., Gao, G.Z., Gao, Z., Li, D.H., Shi, J.C., Feng, Y.Y., Qiao, Z.H., 2017. Records of East Asian monsoon activities in Northeastern China since 15.6 ka, based on grain size analysis of peaty sediments in the Changbai Mountains. Quat. Int. 447, 158–169. https://doi.org/10.1016/j.quaint.2017.03.064.

Li, T.Y., Zhang, J.F., Wu, Y.Q., Du, S.S., Mo, D.W., Liao, Y.N., Chen, Z.T., Liu, J.B., Li, Q., 2020. Holocene aeolian activities linked to indian summer monsoon in the middle reaches of the Yarlung Zangbo River. J. Geogr. Sci. 30, 2002–2014. https://doi.org/10.1007/s11442-020-1824-6.

Li, Y., Han, L., Liu, X.Q., Song, Y.G., Wang, Y.X., 2021. Correlation and anti-correlation of the asian summer monsoon and westerlies during the Holocene. Gondwana Res. 91, 112–120. https://doi.org/10.1016/j.gr.2020.12.013.

Li, Y., Morrill, C., 2015. A Holocene East asian winter monsoon record at the southern edge of the Gobi Desert and its comparison with a transient simulation. Clim. Dyn. 45, 1219–1234. https://doi.org/10.1007/s00382-014-2372-5.

Li, Y., Song, Y., Yin, Q., Han, L., Wang, Y., 2019. Orbital and millennial northern mid-latitude westerlies over the last glacial period. Clim. Dyn. 53, 3315–3324. https://doi.org/10.1007/s00382-019-04704-5.

Li, Y., Wang, N.A., Li, Z.L., Zhou, X.H., Zhang, C.Q., 2012. Holocene climate Cycles in Northwest margin of Asian Monsoon. Chin. Geogr. Sci. 22, 450–461. https://doi.org/10.1007/s11769-012-0551-z.

Liu, B., Jin, H.L., Sun, Z., Miao, Y.F., Su, Z.Z., Zhang, C.X., 2014. Evidence of Holocene millennial-scale climatic change from Gonghe Basin peat deposit, northeastern Qinghai-Tibet Plateau. J. Arid Environ. 106, 1–10. https://doi.org/10.1016/j.jaridenv.2014.03.003.

Liu, D.S., 1985. Loess and Environment (In Chinese). Beijing Science Press, Beijing.

Liu, X., Zhou, X., Zhan, T., Zhou, X., Wu, H., Jiang, S., Tu, L., Oyebanji, D., Shen, Y., 2023. Pollen evidence for a wet Younger Dryas in northern NE China. Catena 220, 106667. https://doi.org/10.1016/j.catena.2022.106667.

Liu, X.X., Sun, Y.B., Vandenberghe, J., Cheng, P., Zhang, X., Gowan, E., Lohmann, G., An, Z.S., 2020. Centennial- to millennial-scale monsoon changes since the last deglaciation linked to solar activities and North Atlantic cooling. Clim. Past. 16, 315–324. https://doi.org/10.5194/cp-16-315-2020.

López-Avilés, A., Jiménez-Moreno, G., García-Alix, A., García-García, F., Camuera, J., Scott Anderson, R., Sanjurjo-Sánchez, J., Arce Chamorro, C., Carrión, J.S., 2022. Post-glacial evolution of alpine environments in the western Mediterranean region: the Laguna Seca record. Catena 211, 106033. https://doi.org/10.1016/j.catena.2022.106033.

Lu, H.Y., Huissteden, K.V., Zhou, J., Vandenberghe, J., Liu, X.D., An, Z.S., 2000. Variability of East Asian Winter Monsoon in Quaternary Climatic Extremes in North China. Quat. Res. 54, 321–327. https://doi.org/10.1006/qres.2000.2173.

Lu, H.Y., Zhao, C.F., Mason, J., Yi, S.W., Zhao, H., Zhou, Y.L., Ji, J.F., Swinehart, J., Wang, C.M., 2011. Holocene climatic changes revealed by aeolian deposits from the Qinghai Lake area (northeastern Qinghai-Tibetan Plateau) and possible forcing mechanisms. The Holocene 21, 297–304. https://doi.org/10.1177/0959683610378884.

Martini, I.P., Cortizas, A.M., Chesworth, W., 2006. Chapter 1 Peatlands: a concise guide to the volume. Dev. Earth Surf. Process. 9, 1–13. https://doi.org/10.1016/S0928-2025(06)09001-8.

Mayewski, P.A., Rohling, E.E., Curt Stager, J., Karlén, W., Maasch, K.A., David Meeker, L., Meyerson, E.A., Gasse, F., van Kreveld, S., Holmgren, K., Lee-Thorp, J., Rosqvist, G., Rack, F., Staubwasser, M., Schneider, R.R., Steig, E.J., 2004. Holocene climate Variability. Quat. Res. 62, 243–255. https://doi.org/10.1016/j.yqres.2004.07.001.

Mischke, S., Zhang, C., 2010. Holocene cold events on the Tibetan Plateau. Glob. Planet. Change 72, 155–163.

Morlet, J., 1982. Wave propagation and sampling theory. Geophysics 47, 203–236. https://doi.org/10.1190/1.1441329.

Nan, Q., Li, T., Chen, J., Chang, F., Yu, X., Xu, Z., Pi, Z., 2017. Holocene paleoenvironment changes in the northern Yellow Sea: evidence from alkenone-derived sea surface temperature. Palaeogeogr. Palaeoclimatol. Palaeoecol. 483, 83–93. https://doi.org/10.1016/j.palaeo.2017.01.031.

Ning, D.L., Jiang, Q.F., Ji, M., Xu, Y.C., Kuai, X., Ge, Y., Zhao, W.W., 2022. Holocene hydroclimate changes on the north-eastern Tibetan Plateau inferred from geochemical records in Lake Gyaring. J. Quat. Sci. 37, 516–526. https://doi.org/10.1002/jqs.3383.

Paterson, G.A., Heslop, D., 2015. New methods for unmixing sediment grain size data. Geochemistry 16, 4494–4506. https://doi.org/10.1002/2015GC006070.

Peng, H.J., Bao, K.S., Yuan, L.G., Uchida, M., Cai, C., Zhu, Y.X., Hong, B., Guo, Q., Ding, H.W., Yao, H., Hong, Y.T., 2021. Abrupt climate variability since the last deglaciation based on a high-resolution peat dust deposition record from Southwest China. Quat. Sci. Rev. 252, 106749 https://doi.org/10.1016/j.quascirev.2020.106749.

Prins, M.A., Vriend, M., 2007. Glacial and interglacial eolian dust dispersal patterns across the Chinese Loess Plateau inferred from decomposed loess grain-size records. Geochem. Geophy. Geosy. 8 https://doi.org/10.1029/2006GC001563.

Pye, K., 1995. The nature, origin and accumulation of loess. Quat. Sci. Rev. 14, 653–667. https://doi.org/10.1016/0277-3791(95)00047-X.

Reimer, P.J., Bard, E., Bayliss, A., Beck, J.W., Blackwell, P.G., Ramsey, C.B., Buck, C.E., Cheng, H., Edwards, R.L., Friedrich, M., 2013. IntCal13 and Marine13 radiocarbon age calibration curves 0–50,000 years cal BP. Radiocarbon 55 (4), 1869–1887. https://doi.org/10.2458/azu_js_rc.55.16947.

Russell, J.M., Johnson, T.C., Talbot, M.R., 2003. A 725 yr cycle in the climate of Central Africa during the late Holocene. Geology 31, 677–680. https://doi.org/10.1130/G19449.1.

Sun, D.H., Su, R.X., Bloemendal, J., Lu, H.Y., 2008. Grain-size and accumulation rate records from late Cenozoic aeolian sequences in northern China: Implications for variations in the East asian winter monsoon and westerly atmospheric circulation. Palaeogeogr. Palaeoclimatol. Palaeoecol. 264, 39–53. https://doi.org/10.1016/j.palaeo.2008.03.011.

Sun, G.Y., Luo, X.Z., Turner, R.E., 2001. A study on peat deposition Chronology of Holocene of Zorge Plateau in the Northeast Qinghai-Tibetan Plateau. Acta Sedimentol. Sin. 19, 177–181 (in Chinese with English abstract).doi:

Sun, X.H., Zhao, Y., Li, Q., 2017. Holocene peatland development and vegetation changes in the Zoige Basin, eastern Tibetan Plateau. Sci. China Earth Sci. 60, 1826–1837. https://doi.org/10.1007/s11430-017-9086-5.

Sun, Y.B., Clemens, S.C., Morrill, C., Lin, X.P., Wang, X.L., An, Z.S., 2012. Influence of Atlantic meridional overturning circulation on the East asian winter monsoon. Nat. Geosci. 5, 46–49. https://doi.org/10.1038/NGEO1326.

Sun, Y.B., Wang, X.L., Liu, Q.S., Clemens, S.C., 2010. Impacts of post-depositional processes on rapid monsoon signals recorded by the last glacial loess deposits of northern China. Earth Planet. Sci. Lett. 289, 171–179. https://doi.org/10.1016/j.epsl.2009.10.038.

Vandenberghe, J., 2013. Grain size of fine-grained windblown sediment: a powerful proxy for process identification. Earth Sci. Rev. 121, 18–30. https://doi.org/10.1016/j.earscirev.2013.03.001.

Vriend, M., Prins, M.A., Buylaert, J.-P., Vandenberghe, J., Lu, H., 2011. Contrasting dust supply patterns across the north-western Chinese Loess Plateau during the last glacial-interglacial cycle. Quat. Int. 240, 167–180. https://doi.org/10.1016/j.quaint.2010.11.009.

Wang, H., Hong, Y.T., Lin, Q.H., Hong, B., Zhu, Y.X., Wang, Y., Xu, H., 2010. Response of humification degree to monsoon climate during the Holocene from the Hongyuan peat bog, eastern Tibetan Plateau. Palaeogeogr. Palaeoclimatol. Palaeoecol. 286, 171–177. https://doi.org/10.1016/j.palaeo.2009.12.015.

Wang, J.M., Pan, B.T., 1997. Loess deposition eastern part of Qinghai-Xizang Plateau: its characteristics and environment. J. Desert Res. 17, 395–402 (in Chinese with English abstract).http://doi.org/CNKI:SUN:ZGSS.0.1997-04-009.

Wang, Q.F., Jin, H.J., Wu, Q.B., Liu, B., 2020. A 7-ka climatic variability record inferred from peat bog sediments in the north of Bayan Har Mountains, northeastern Tibetan Plateau. Environ. Earth Sci. 79, 156. https://doi.org/10.1007/s12665-020-8897-5.

Wang, Y., Wang, S., Xue, B., Lei, J.I., Jinglu, W.U., Xia, W., Pan, H., Zhang, P., Chen, F., 1995. Sedimentological evidence of the piracy of fossil Zoige Lake by the Yellow River. Chin. Sci. Bull. 40, 1539–1544. https://doi.org/10.1007/BF02253378.

Weltje, G.J., 1997. End-member modeling of compositional data: Numerical-statistical algorithms for solving the explicit mixing problem. Math. Geol. 29, 503–549. https://doi.org/10.1007/BF02775085.

Wen, X.Y., Liu, Z.Y., Wang, S.W., Cheng, J., Zhu, J., 2016. Correlation and anti-correlation of the East asian summer and winter monsoons during the last 21,000 years. Nat. Commun. 7, 11999. https://doi.org/10.1038/ncomms11999.

Xian, F., Zhou, W.J., Yu, X.F., Lu, X.F., Lars, G.F., 2006. Evidence for abrupt changes of the asian monsoon during the Holocene:from the heat records of Tibetan plateau. Mar. Geol. Quat. Geol. 26, 41–45 (in Chinese with English abstract).doi:10.16562/j.cnki.0256-1492.2006.01.007.

Xiao, S.B., Li, A.C., Liu, J.P., Chen, M.H., Xie, Q., Jiang, F.Q., Li, T.G., Xiang, R., Chen, Z., 2006. Coherence between solar activity and the East asian summer monsoon variability in the past 8000 years from Yangtze River-derived mud in the East China Sea. Palaeogeogr. Palaeoclimatol. Palaeoecol. 237, 293–304. https://doi.org/10.1016/j.palaeo.2005.12.003.

Xie, H.C., 2019. Climate change characteristics in the Asian Westerlies dominated area recorded by geochemical proxies during late Quaternary (in Chinese). In: Lanzhou University, p. 162.

Yan, D., Wünnemann, B., Zhang, Y., Long, H., Stauch, G., Sun, Q., Cao, G., 2018. Response of lake-catchment processes to Holocene climate variability: Evidences from the NE Tibetan Plateau. Quat. Sci. Rev. 201, 261–279. https://doi.org/10.1016/j.quascirev.2018.10.017.

Yan, T.L., Zhao, C., Yan, H., Ge, S., Sun, X.S., Zhang, C., Feng, X.P., Leng, C.C., 2021. Elevational differences in Holocene thermal maximum revealed by quantitative temperature reconstructions at ~30° N on eastern Tibetan Plateau. Palaeogeogr. Palaeoclimatol. Palaeoecol. 570, 110364 https://doi.org/10.1016/j.palaeo.2021.110364.

Yang, X.L., Yang, H., Wang, B.Y., Huang, L.J., Shen, C.C., Edwards, R.L., Cheng, H., 2019. Early-Holocene monsoon instability and climatic optimum recorded by chinese stalagmites. The Holocene 29, 1059–1067. https://doi.org/10.1177/0959683619831433.

Yu, X.F., Liu, Z., 2010. Surface texture and mineralogical characters of the peat in Hongyuan Swamp (in Chinese with English abstract). Earth Environ. 1, 122–125.

Yu, X.F., Zhou, W.J., Liu, Z., Kang, Z.H., 2011. Different patterns of changes in the asian summer and winter monsoons on the eastern Tibetan Plateau during the Holocene. The Holocene 21, 1031–1036. https://doi.org/10.1177/0959683611400460.

Zaccone, C., Miano, T.M., Shotyk, W., 2012. Interpreting the ash trend within ombrotrophic bog profiles: atmospheric dust depositions vs. Mineralization processes. The Etang de la Gruere case study. Plant Soil 353, 1–9. https://doi.org/10.1007/s11104-011-1055-9.

Zeng, M.X., Zeng, Q., Peng, H.J., Wu, Y.Q., Li, Y., Song, Y.G., Sheng, E.G., Wu, Y.Y., Wang, T.Y., Ni, J., 2022. Late Holocene hydroclimatic changes inferred from a karst peat archive in the western Guizhou Plateau, SW China. J. Asian Earth Sci. 229, 105179 https://doi.org/10.1016/j.jseaes.2022.105179.

Zeng, M.X., Zhu, C., Song, Y., Ma, C., Yang, Z., 2017. Paleoenvironment change and its impact on carbon and nitrogen accumulation in the Zoige wetland, northeastern Qinghai-Tibetan Plateau over the past 14,000 years. Geochem. Geophy. Geosy. 18, 1775–1792. https://doi.org/10.1002/2016GC006718.

Zeng, M.X., Zhu, C., Song, Y.G., Wu, Y.Q., Wang, H.J., Zhang, Y.W., He, K.Y., Chen, J., Wu, Z.R., Zeng, Q., 2022. Significance of fluvial landform evolution and river reorganization in settlement development over the past 50 ka: A case study of Baodun site on Chengdu Plain, SW China. Geomorphology 409, 108267. https://doi.org/10.1016/j.geomorph.2022.108267.

Zhang, D.L., Feng, Z.D., 2018. Holocene climate variations in the Altai Mountains and the surrounding areas: A synthesis of pollen records. Earth Sci. Rev. 185, 847–869. https://doi.org/10.1016/j.earscirev.2018.08.007.

Zhang, P., Song, C.H., Yang, Y.B., Gao, H.S., Zhang, H.Y., Liu, W.M., Pan, M.H., Liu, P., Hu, S.H., Xia, W.M., 2008. The significance and Establishment of Discriminant Function with grain size of Stable Lacustrine Sediment and Eolian Loess. Acta Sedimentol. Sin. 26, 501–507 (in Chinese with English abstract).http://doi.org/CNKI:SUN:CJXB.0.2008-03-018.

Zhao, J.H., Wang, D., Yu, L.H., Zhang, X.Y., Yang, L.I., Yan, L.W., 2006. Variations of Geochemical Elements in Xining Loess Deposit and the Paleoclimatic Implications. J. Arid Land Resour. Environ. 20, 104–108. https://doi.org/10.1111/j.1745-4557.2006.00081.x (in Chinese with English abstract).

Zhao, K., Wang, Y.J., Edwards, R.L., Cheng, H., Liu, D.B., Kong, X.G., Ning, Y.F., 2016. Contribution of ENSO variability to the East asian summer monsoon in the late Holocene. Palaeogeogr. Palaeoclimatol. Palaeoecol. 449, 510–519. https://doi.org/10.1016/j.palaeo.2016.02.044.

Zhao, Y., Tang, Y., Yu, Z., Li, H., Yang, B., Zhao, W., Li, F., Li, Q.J.T.H., 2014. Holocene peatland initiation, lateral expansion, and carbon dynamics in the Zoige Basin of the eastern Tibetan Plateau. The Holocene 24, 1137–1145. https://doi.org/10.1177/0959683614538077.

Zhou, W.J., Yu, S.Y., Burr, G.S., Kukla, G.J., Jull, A.J.T., Xian, F., Xiao, J.Y., Colman, S.M., Yu, H.G., Liu, Z., Kong, X.H., 2010. Postglacial changes in the asian summer monsoon system: a pollen record from the eastern margin of the Tibetan Plateau. Boreas 39, 528–539. https://doi.org/10.1111/j.1502-3885.2010.00150.x.